PAPER

Advances in understanding of high-*Z* material erosion and re-deposition in low-*Z* wall environment in DIII-D

IOP Publishing | International Atomic Energy Agency Nuclear Fusion

Nucl. Fusion **57** (2017) 056016 (8pp) https://doi.org/10.1088/1741-4326/aa6451

Advances in understanding of high-*Z* material erosion and re-deposition in low-*Z* wall environment in DIII-D

R. Ding[1,2,3], D.L. Rudakov[4], P.C. Stangeby[5], W.R. Wampler[6], T. Abrams[3], S. Brezinsek[7], A. Briesemeister[8], I. Bykov[4], V.S. Chan[3], C.P. Chrobak[3], J.D. Elder[5], H.Y. Guo[3], J. Guterl[1], A. Kirschner[7], C.J. Lasnier[9], A.W. Leonard[3], M.A. Makowski[9], A.G. McLean[9], P.B. Snyder[3], D.M. Thomas[3], D. Tskhakaya[10], E.A. Unterberg[8], H.Q. Wang[1] and J.G. Watkins[6]

[1] Oak Ridge Associated Universities, Oak Ridge, TN, United States of America
[2] Institute of Plasma Physics, Chinese Academy of Sciences, PO Box 1126, Hefei, Anhui 230031, People's Republic of China
[3] General Atomics, PO Box 85608, San Diego, CA 92186-5608, United States of America
[4] University of California San Diego, 9500 Gilman Drive, La Jolla, CA 92093-0417, United States of America
[5] University of Toronto, Institute for Aerospace Studies, Toronto, M3H 5T6, Canada
[6] Sandia National Laboratory, PO Box 5800, Albuquerque, NM 87185, United States of America
[7] Forschungszentrum Jülich GmbH, Institute of Energy and Climate Research-Plasma Physics, Partner of the Trilateral Euregio Cluster (TEC), 52425, Jülich, Germany
[8] Oak Ridge National Lab, Oak Ridge, TN, United States of America
[9] Lawrence Livermore National Laboratory, 7000 East Avenue, Livermore, CA 94550, United States of America
[10] Fusion@ÖAW, Institute of Applied Physics, TU Wien, Wiedner Hauptstraße 8-10, 1040 Vienna, Austria

E-mail: rding@ipp.ac.cn

Received 20 December 2016, revised 18 February 2017
Accepted for publication 3 March 2017
Published 24 March 2017

Abstract

Dedicated DIII-D experiments coupled with modeling reveal that the net erosion rate of high-*Z* materials, i.e. Mo and W, is strongly affected by carbon concentration in the plasma and the magnetic pre-sheath properties. Different methods such as electrical biasing and local gas injection have been investigated to control high-*Z* material erosion. The net erosion rate of high-*Z* materials is significantly reduced due to the high local re-deposition ratio. The ERO modeling shows that the local re-deposition ratio is mainly controlled by the electric field and plasma density within the magnetic pre-sheath. The net erosion can be significantly suppressed by reducing the sheath potential drop. A high carbon impurity concentration in the background plasma is also found to reduce the net erosion rate of high-*Z* materials. Both DIII-D experiments and modeling show that local $^{13}CH_4$ injection can create a carbon coating on the metal surface. The profile of ^{13}C deposition provides quantitative information on radial transport due to $\mathbf{E} \times \mathbf{B}$ drift and the cross-field diffusion. The deuterium gas injection upstream of the W sample can reduce W net erosion rate by plasma perturbation. In H-mode plasmas, the measured inter-ELM W erosion rates at different radial locations are well reproduced by ERO modeling taking into account charge-state-resolved carbon ion flux in the background plasma calculated using the OEDGE code.

Keywords: erosion, deposition, high-*Z* materials, impurity

(Some figures may appear in colour only in the online journal)

1. Introduction

High-*Z* plasma facing materials (PFMs) have the distinct advantages of longer lifetime and lower fuel retention compared to low-*Z* PFMs. The most promising high-*Z* material tungsten (W) has been selected as the PFM for the divertor of ITER [1] and will potentially be used in future fusion devices. The main challenge for high-*Z* materials is large radiation losses and fuel dilution caused by high-*Z* impurities transported into the core plasma, resulting in degraded plasma performance. It is estimated that the maximum tolerable central W concentration in ITER is only a few times 10^{-5} [2]. One way to limit the core W concentration is to control the W source in the divertor. Therefore, it is essential to understand and control high-*Z* material erosion and re-deposition in fusion devices.

In tokamak experiments, the most fundamental erosion mechanism for high-*Z* materials is physical sputtering by impinging ions. Since high-*Z* materials have a higher sputtering threshold energy, the sputtering rates are often determined by impurities instead of the fuel ions, especially in a mixed material environment. The JET ITER-like wall experiments show that W sputtering is mainly due to bombardment by beryllium ions originating from the main chamber wall for a wide range of plasma conditions [3]. Only in the H-mode discharges with higher pedestal electron temperatures, the intra-ELM W sputtering by fuel species becomes important [4]. In ASDEX Upgrade, the carbon impurity is mainly responsible for the divertor W source [5]. Another critical feature for high-*Z* materials is the high local redeposition probability of eroded materials due to their fast ionization and large gyroradius, which significantly reduces the effective impurity source [6, 7]. The lifetime of PFMs and core impurity level are determined by the net erosion, defined as the difference between gross erosion and redeposition. It has been found that high-*Z* materials have much lower net erosion rates than gross erosion rates in different tokamaks [8, 9].

Since the DIII-D tokamak has full graphite PFMs, high-*Z* material erosion and redeposition can be studied in a mixed materials environment, in which low-*Z* carbon impurities in the plasma play an important role. The divertor materials evaluation system (DiMES) [10] in the lower divertor of DIII-D provides a flexible platform for material erosion studies with a comprehensive set of edge diagnostics, including divertor target Langmuir probes, divertor Thomson scattering and emission spectroscopy measuring the local plasma conditions. Well controlled sample exposure combined with post-mortem ion beam analysis provides the opportunity to advance code validation. Within this work, dedicated experiments coupled with modeling have identified the critical parameters determining high-*Z* material erosion such as the magnetic pre-sheath properties and background impurities. In addition, erosion control has been successfully demonstrated in DIII-D using different methods.

2. DiMES experiments at DIII-D

The thin film samples of high-*Z* materials, molybdenum (Mo) or W, were inserted flush with the lower divertor tiles of DIII-D and exposed to well-diagnosed plasma conditions using the DiMES manipulator. High-*Z* coatings of dozens of nm thick were deposited in a magnetron sputter deposition system. Several DiMES heads with W or Mo samples for different experiments are shown in figure 1. All the high-*Z* coatings are of circular shape and surrounded by either graphite or a carbon coating on a silicon substrate. Lower single null magnetic configurations with the deuterium plasma were employed for all the experiments, in which the outer strike point (OSP) was placed close to the sample during the plasma current flattop to ensure net erosion conditions on the samples. The electron density and temperature profiles near the OSP were measured by the divertor Langmuir probes and divertor Thomson scattering.

At the top of the machine, a filtered camera cross-calibrated with a high-resolution spectrometer provides *in situ* measurements of the gross erosion rate using the inverse photon efficiency, the so-called S/XB value. This parameter converts photon fluxes into particle fluxes of eroded atoms [11, 12]. The net erosion rate can be determined by measuring the coating thickness of the high-*Z* material sample before and after the plasma exposure using Rutherford backscattering (RBS) [13]. A non-spectroscopic method to measure gross erosion rate has been developed by measuring the net erosion rate of a tiny coating spot [9, 14]. If the coating size is small enough, the redeposition of eroded material on its source location will be negligible. Since the ionization length of sputtered neutrals is on the order of mm under the typical DIII-D divertor condition, the redeposition of eroded material on the 1 mm spot can be neglected according to the modeling results [15, 16]. Therefore, gross and net erosion rates were measured by simultaneous exposure of both 1 mm and 1 cm diameter samples. As shown in figure 1, the 1 mm sample is located upstream of the 1 cm sample to minimize the redeposition on 1 mm sample from 1 cm sample. The ratio of erosion of 1 cm sample to 1 mm sample gives the net/gross erosion ratio. The redeposition ratio, defined as the number of particles redeposited on their original surface divided by the total number of eroded particles, can also be calculated. Different samples have been exposed to DIII-D plasma to identify the main controlling physics with the aid of modeling.

3. The model

The 3D Monte Carlo code ERO [17], has been used to model the high-*Z* material erosion and redeposition for different DiMES experiments. The ERO code simulates the plasma material interaction and local impurity transport in a given background plasma condition. Both physical sputtering and chemical erosion are included. The eroded particles are then traced until they are redeposited or move deeper into the plasma, after which they are no longer followed. Different atomic and molecular processes, electromagnetic force and friction force for charged particles are taken into account. The main input required for ERO modeling is the plasma background which is reconstructed by the interpretive OEDGE code using the Onion Skin Model

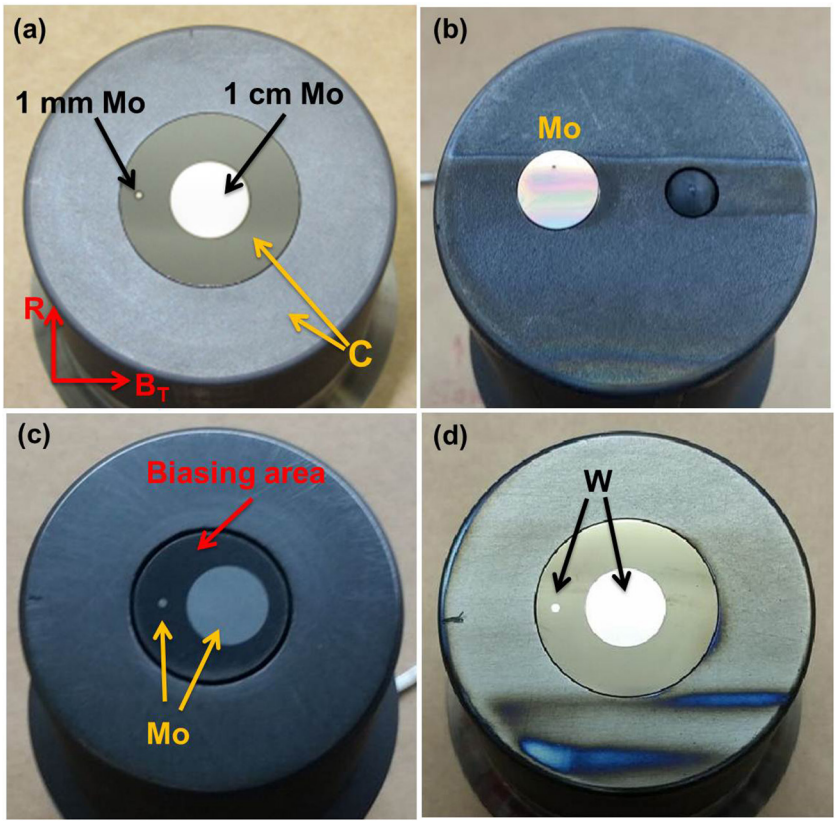

Figure 1. Photographs of various samples for different experiments: (*a*) Mo sample for gross and net erosion measurements, (*b*) Mo sample after exposure with methane injection, (*c*) Mo sample for electrical biasing and (*d*) W sample after exposure with deuterium injection.

(OSM) [18]. The OEDGE code solves the 1D fluid continuity equations along the magnetic field with the input boundary condition of plasma parameters on divertor targets measured by edge diagnostics. The plasma density, temperature, flow velocity and electric field on a 2D grid representing the poloidal magnetic structure are then used for the local 3D grid of ERO simulations with assumption of toroidal symmetry. Figure 2 shows the poloidal cross-section of DIII-D lower divertor with ERO simulation volume. The DiMES center is at the bottom center of the ERO simulation volume.

A material mixing model has been taken into account in the ERO code to handle the effect of mixing of carbon with high-*Z* materials in the material surface [19]. In the model, the erosion and deposition of different species only take place in an interaction layer, which is on top of the substrate material surface. The total number of particles in the interaction layer is kept constant with a homogeneous distribution of different species. Under net-erosion conditions, lost particles are replenished with particles from the substrate volume. If net-deposition occurs, excess particles are moved into the substrate volume according to the relative concentrations of different species inside the interaction layer. When the surface reaches steady state composition, the elemental concentrations in the interaction layer do not change anymore with increasing simulation time. The erosion and deposition of different materials at steady state can then be obtained and compared with experimental measurements.

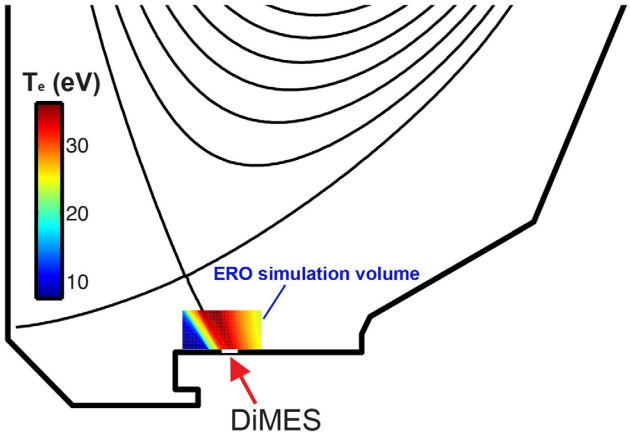

Figure 2. ERO simulation volume with 2D distribution of electron temperature obtained from OEDGE modeling as input.

4. Results and discussions

4.1. Effect of sheath

With simultaneous exposure of 1 cm and 1 mm samples as shown in figure 1(*a*), the previously measured redeposition ratio of the 1 cm sample is 44% for Mo and 63% for W [14]. The net erosion rate of high-*Z* materials is found to be significantly reduced due to a high local re-deposition ratio. According to the modeling with the ERO code, the local re-deposition ratio is mainly controlled by the electric field and electron density within the magnetic pre-sheath [15]. In the

experiments, the magnetic field lines intersect the DiMES sample surface at a very shallow angle of 1.5°. Normally, the magnetic pre-sheath potential drop is increased when the angle between the magnetic field lines and the material surface is reduced [20, 21]. Recent fluid analysis suggests that the Debye sheath can even disappear when the angle is small enough, and the entire sheath potential is equal to the magnetic pre-sheath potential [22]. Most of the sputtered Mo and W atoms are ionized within the magnetic pre-sheath region and therefore the strong electric field towards the material surface can easily draw the sputtered particles back to the surface. If the sheath electric field is not taken into account in the ERO modeling, the Mo redeposition ratio is reduced significantly, as shown in figure 3. With the sheath electric field, the modelled Mo redeposition ratio is 39% for 1 cm, close to the experimental value. The Mo redeposition ratio is only 4% for 1 mm sample. With increasing the sample diameter, the Mo redeposition ratio also increases. The ERO modeling shows that the higher redeposition ratio for W compared to that for Mo is mainly due to the shorter ionization mean free path of sputtered W atoms.

The ERO simulations find that the Mo redeposition ratio is not reduced when the sheath potential drop is decreased. For a non-floating material surface with different sheath potentials, the potential profile can be calculated by solving the fluid equations [22], including the particle and momentum conservative equations and the Boltzmann relation. Although the sheath electric field is decreased for lower total potential drop, the electron density within the magnetic pre-sheath increases according to the Boltzmann relation. Therefore, the ionization length becomes shorter due to higher electron density, which enhances the redeposition. The changes in the sheath electric field and electron density within the magnetic pre-sheath have opposite effects on the redeposition ratio. Decreasing the sheath potential drop also results in a lower gross erosion rate because the sputtering yield is reduced due to the lower ion incident energy on the surface. Therefore the Mo net erosion rate can be strongly reduced by positive biasing relative to the floating potential, since the Mo redeposition ratio is not decreased.

Controlled experiments have been performed to study the influence of external biasing on Mo erosion. As shown in figure 1(*c*), the central part of DiMES with a diameter of 1.9 cm including both 1 cm and 1 mm Mo coatings is isolated and can be biased with an external power supply. In the experiments, biasing voltage was swept with different frequency and waveform. The Mo gross erosion was measured by a fast camera with a Mo I filter at 550 nm. Two additional identical samples with fixed biasing voltage of 39 V or floating potential were exposed for post-mortem surface analysis to obtain the erosion rates. Since the measured local electron temperature is about 30 eV, the 39 V biasing voltage is much lower than the plasma potential. For the fixed positive biasing voltage, a rapid switch back to negative voltage of -6 V with a frequency of 10 Hz was made to avoid arcing.

As seen from figure 4(*a*), the measured Mo I emission, i.e. the Mo gross erosion rate, shows a clear modulation at the biasing voltage sweeping frequency. With negative biasing,

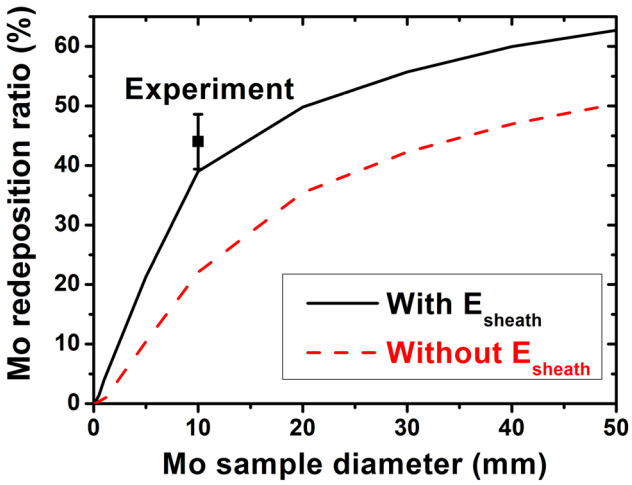

Figure 3. The dependence of the ERO simulated Mo redeposition ratio on sample diameter with and without sheath electric field E_{sheath} compared with experiment.

the Mo erosion rate attains the highest value, while positive biasing leads to minimum Mo erosion. Figure 4(*b*) compares the Mo I emission for positive biasing voltage with that for a floating surface. The Mo I emission is reduced by more than an order of magnitude with 39 V biasing voltage. The spikes for the 39 V bias are probably due to the quick switch back to negative voltage periodically. The Mo erosion of the 1 mm sample from RBS measurements is 9.5×10^{16} atoms cm^{-2} for the floating sample, while for the positive biased sample the Mo erosion is below the RBS detection limit of 0.6×10^{16} atoms cm^{-2}. The Mo erosion is strongly suppressed with positive biasing.

4.2. Effect of low-Z impurities

The intrinsic low-*Z* carbon impurities in DIII-D play an important role in high-*Z* material erosion. According to the ERO simulations using a material mixing model [15], higher carbon impurity concentrations in the plasma can reduce the net erosion rate of Mo. More carbon in the background plasma leads to more carbon deposited in the mixed material surface layer. Therefore, the effective sputtering rate of Mo is reduced due to surface dilution. The measured Mo and W net erosion rates are well reproduced by ERO modeling assuming a carbon concentration of 1.8%, which is within the uncertainty of experimental estimates based on low charge state carbon emissions. If the carbon concentration in the plasma is high enough, net deposition will occur on the material surface, and high-*Z* material will be covered by deposited carbon layer.

The local background carbon concentration can be increased by methane injection close to the DiMES sample. During the Mo sample exposure, methane gas was injected through a capillary to a hole in a divertor tile at the same major radius as the DiMES center and 12 cm upstream of it in the toroidal direction [23]. ^{13}C labelled methane was used for injection to distinguish the injected carbon from the background ^{12}C in post-mortem analysis. Three Mo samples have been exposed with $^{13}CH_4$ injection, four L-mode discharges for the first sample, two H-mode discharges for

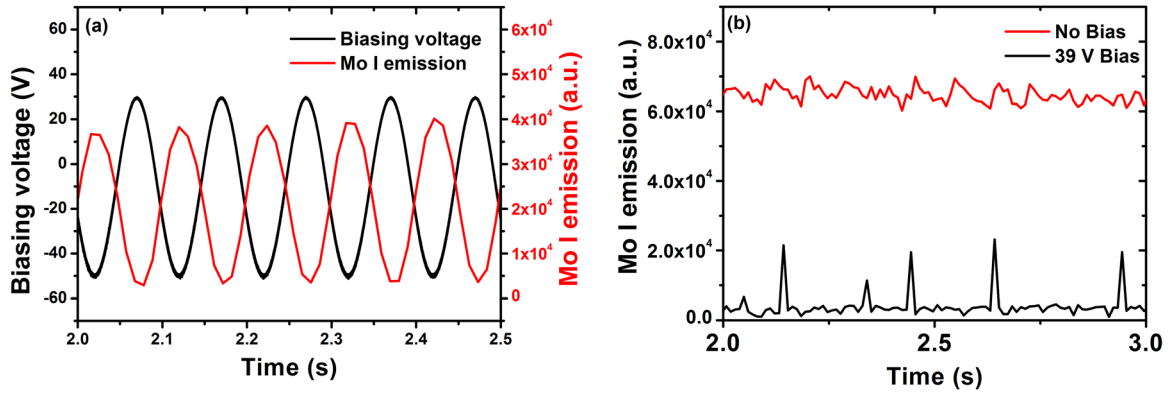

Figure 4. Measured Mo I emission for different biasing voltage: (*a*) sine wave from -50 V to 30 V and (*b*) floating versus fixed positive bias of 39 V.

the second sample and three L-mode discharges for the third sample. Measurements by the multichord divertor spectrometer (MDS) show that Mo I emission was reduced significantly when $^{13}CH_4$ injection started, which indicates that Mo erosion was suppressed. During the first Mo exposure, the methane injection rate was not stable, while the plasma condition during ELMs was hard to be determined in the second H-mode experiment. The third Mo exposure was carried out at constant reproducible L-mode conditions suitable for the model validation. The Mo I emission was reduced to the noise background level during methane injection. The $^{13}CH_4$ injection rate was kept at about 1.8 Torr-l s^{-1} for the three repeat discharges. After the experiment, carbon deposition could be clearly seen as a toroidal stripe on the DiMES head, as shown in figure 1(*b*). The 1 cm Mo sample coating was located 1 cm upstream from the DiMES center in order to accommodate an embedded Langmuir probe. The Mo sample experienced a net-deposition condition due to the gas injection and this resulted in Mo erosion below the detection limit of post-mortem RBS measurements. The carbon deposition on the Mo sample was measured by nuclear reaction analysis (NRA) with 2.5 MeV ^{3}He ion beam. The average total carbon ($^{13}C + {}^{12}C$) deposition rate was about 47 nm s^{-1} with about 90% of ^{13}C in the C deposited layer. Therefore, the carbon deposition was mainly due to high carbon concentration in the plasma induced by the external gas injection.

The measured ^{13}C deposition profile on the Mo sample provides a good benchmark for the ERO code. In the ERO modeling, methane molecules are launched at the injection hole with a cosine angular distribution and Maxwellian energy distribution. The ionization and dissociation of methane molecules are calculated using the corresponding reaction rate coefficients [24]. The effective sticking coefficient for hydrocarbon molecules hitting material surfaces is assumed to be 0, in accord with previous studies [25]. It is found that the ERO modelled radial coverage of ^{13}C strongly depends on $\mathbf{E} \times \mathbf{B}$ drifts and the cross-field diffusion coefficient. As shown in figure 5, if both the sheath electric field E and the diffusion coefficient D are assumed to be 0, the radial ^{13}C deposition profile is rather symmetric relative to the radial location of gas injection. When E is taken into account, the modelled deposition profile is shifted in the $\mathbf{E} \times \mathbf{B}$ direction, which indicates

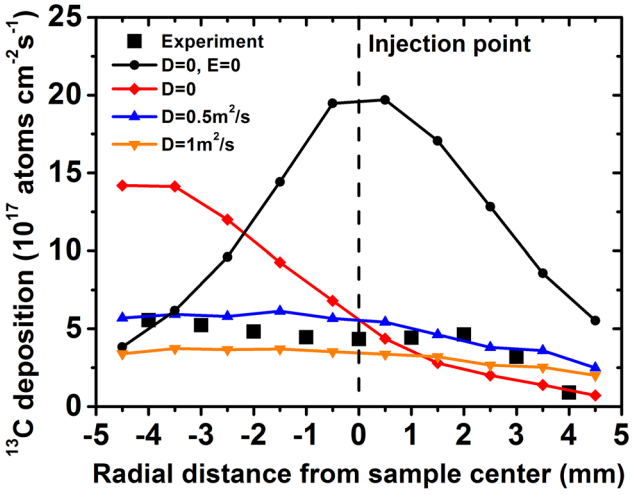

Figure 5. Comparison of experimental and ERO modelled radial profiles of ^{13}C deposition rates on a Mo sample for different assumptions of the cross-field diffusion coefficients and sheath electric field.

that the higher measured ^{13}C deposition from experiment in the radial inboard direction is mainly due to $\mathbf{E} \times \mathbf{B}$ drift. This is consistent with the conjecture made in [26, 27] on the impact of drift on C migration. A higher diffusion coefficient D leads to lower ^{13}C deposition on the Mo sample and the profile becomes broader, which shows better agreement with the experiments.

4.3. Effect of local plasma conditions

Local deuterium gas injection upstream of the W sample can also reduce the W erosion due to local plasma perturbation. Two identical samples with both 1 cm and 1 mm diameter W coatings were exposed with and without D_2 gas puffing (figure 1(*d*)). The same injection aperture as in previous methane injection experiments was used for D_2 gas injection with a much higher injection rate. Before the sample exposure, a built-in Langmuir probe was installed on the DiMES head and exposed to several repeat discharges with D_2 gas injection in order to measure the local plasma parameters before and during the gas injection. Figure 6 shows the time evolution of different parameters in a typical D_2 gas injection discharge. All the D_2 injection

discharges are reproducible and each of them can be divided into three phases. In the beginning of the discharge, there is no gas injection close to DiMES. The D_2 injection starts at around 2.5 s with an increasing rate to about 9 Torr-l s^{-1}. Finally, the injection rate is increased to a very high level of about 15 Torr-l s^{-1} at 4 s. As shown in figure 6, the gas injection has very little impact on the global discharge parameters, such as plasma current and core plasma density. The embedded Langmuir probe data shows strong local perturbation of electron density and temperature due to the D_2 gas injection. When the gas puff starts, T_e is reduced from about 26 eV to below 10 eV and n_e is increased from about 7.7×10^{12} cm^{-3} to more than 2×10^{13} cm^{-3}. The T_e and n_e are changed slightly for the highest injection rate compared to the lower injection rate.

The first W-coated sample was exposed for three repeat discharges with the same time evolution of D_2 gas injection as shown in figure 6. The second W-coated sample was exposed for another three repeat discharges without gas injection for comparison. During D_2 gas injection, the W I emission at 400.9 nm measured by MDS was reduced close to the background noise level. After exposure with D_2 gas injection, there is a visible carbon deposited layer at the radial inboard side of the W coating, as shown in figure 1(*d*). No visible carbon deposition is found on the sample without gas injection. The local plasma perturbation by gas injection changes the balance of carbon erosion and deposition and leads to more carbon deposition. According to the RBS measurements, the W erosion without gas puffing is about 1.96 ($\pm$0.3) $\times$ 10^{16} atoms cm^{-2} for the 1 mm sample and 1.54 ($\pm$0.3) $\times$ 10^{16} atoms cm^{-2} for the 1 cm sample. With D_2 injection, the W erosion is reduced to about 1.2 ($\pm$0.3) $\times$ 10^{16} atoms cm^{-2} for the 1 mm sample and 0.78 ($\pm$0.3) $\times$ 10^{16} atoms cm^{-2} for the 1 cm sample. The average W net erosion rate for 1 cm sample is reduced by a factor of 2 due to the D_2 gas injection.

ERO simulations have been performed for the three phases: no gas puff ($n_e \sim 7.7 \times 10^{12}$ cm^{-3}, $T_e \sim 26$ eV), low D_2 injection rate ($n_e \sim 2.3 \times 10^{13}$ cm^{-3}, $T_e \sim 9.3$ eV) and high D_2 injection rate ($n_e \sim 2.6 \times 10^{13}$ cm^{-3}, $T_e \sim 7.7$ eV). The carbon concentration in the background plasma is assumed to be 1.8% according to the previous studies. Figure 7(*a*) compares the W net erosion rates for both 1 mm and 1 cm samples between modeling and experiments. For the non-puffing phase, modelled net erosion rates are 0.23 nm s^{-1} for the 1 mm W sample and 0.11 nm s^{-1} for the 1 cm W sample, which are close to the measured values of 0.26 nm s^{-1} for the 1 mm sample and 0.2 nm s^{-1} for the 1 cm sample. The measured net/gross erosion ratio is about 0.77, which indicates the W redeposition ratio for 1 cm sample is only about 23%, much lower than the previous measurement of 63% [14]. The ERO modelled redeposition ratio for the 1 cm sample is 53%, closer to the previous measurement. The error bar from RBS measurements is also larger than previous experiments due to a thicker W film.

With D_2 gas injection, the modelled W net erosion rates of both the 1 cm and 1 mm samples are reduced significantly. Since the D_2 gas injection rate is changed during the discharge, the time-averaged modelled W net erosion rates according to the time proportions of the three phases are used for comparison with the experimental measurements. As shown in figure 6, for a flattop time from 1 s to 5 s, the time for the non-puffing phase, low injection rate phase and high injection rate phase in one discharge is 1.5 s, 1.5 s and 1 s, respectively. Therefore, the time proportions of 37.5%, 37.5% and 25% are used to calculate the average erosion rates. The modelled average W net erosion rates with gas injection are 0.054 nm s^{-1} for the 1 cm sample and 0.12 nm s^{-1} for the 1 mm sample, in fair agreement with the measured values of 0.1 nm s^{-1} for the 1 cm sample and 0.16 nm s^{-1} for the 1 mm sample. The gas injection reduces the local plasma temperature but increases the ion flux, nearly double of that without gas injection. As shown in figure 7(*b*), W sputtering yield by C incidence is decreased significantly for lower plasma temperature in ERO simulations. Furthermore, more carbon is deposited in the mixed material surface layer, which can reduce the W erosion rate as discussed in section 4.2. Therefore, the lower W erosion with D_2 gas puffing is due to both plasma cooling and higher carbon deposition on the W surface. The measured W redeposition ratio with gas injection is increased to about 45%, still lower than the modelled values. The modelled W redeposition ratio is also slightly increased with gas injection, which is mainly due to the shorter ionization mean free path of W atoms resulting from much higher local electron density.

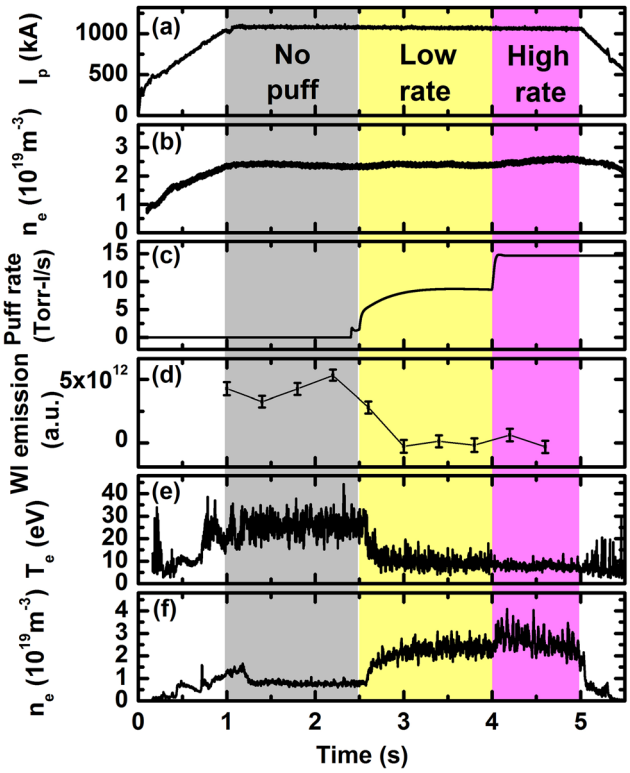

Figure 6. Time traces of typical parameters for D_2 gas injection discharge: (*a*) plasma current, (*b*) line-averaged electron density, (*c*) D_2 injection rate, (*d*) WI emission intensity, (*e*) electron temperature (*f*) and electron density measured by the Langmuir probe embedded in DiMES head.

4.4. Inter-ELM W erosion in H-mode plasma

In situ measurements of the W gross erosion rate in DIII-D H-mode plasma conditions have been carried out with a full W

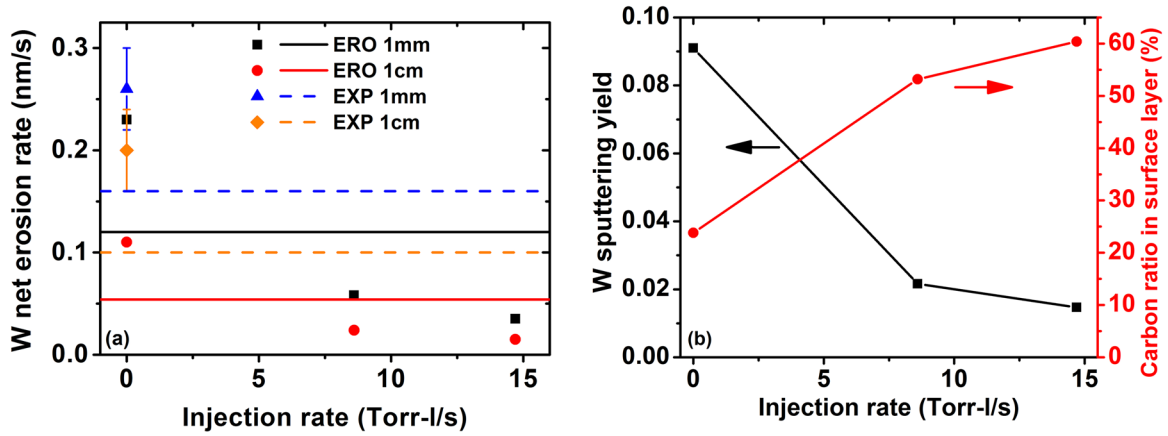

Figure 7. (*a*) Comparison of modelled (ERO) and measured (EXP) W net erosion rates of both 1 mm and 1 cm samples for different injection rates. The average W net erosion rates with D_2 gas injection are marked in solid lines (ERO) and dashed lines (EXP). (*b*) W sputtering yield and ERO modelled carbon ratio in surface interaction layer as a function of gas injection rate.

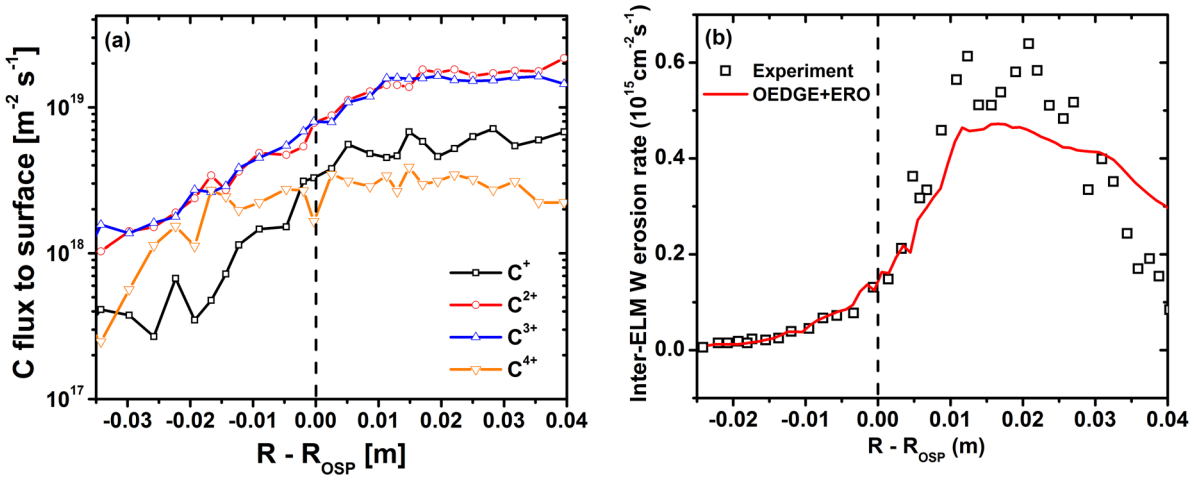

Figure 8. (*a*) OEDGE calculated carbon fluxes in different charge states as a function of radial position. (*b*) Spectroscopic measurements of the inter-ELM W erosion rate as a function of radial position in comparison with OEDGE and ERO modeling.

coating on the DiMES head [28]. The WI 400.9 nm spectral line intensity was measured by a CCD-based camera with 10 ms time resolution and ~0.2 mm spatial resolution, which was calibrated via the MDS with high spectral resolution. The previous experimental data for the S/XB coefficient of WI (400.9 nm) was used to calculate the W gross erosion flux with the measured line emission intensity [11]. The WI emission data is filtered for ELMs using D_α emission data measured by the lower divertor filterscope. In this paper, the inter-ELM W erosion results are used for validation of detailed physics models while ELM induced W erosion will be discussed elsewhere. The OSP was swept slowly inboard and outboard across DiMES during the discharge to obtain different divertor conditions. The radial profile of the inter-ELM W erosion rate is shown in figure 8(*b*).

Since the W sputtering is mainly controlled by carbon impurities in the background plasma, it is important to make a good estimation of the incident carbon flux. The global carbon impurity transport with the OSM background plasma reconstruction is simulated using the DIVIMP code, a portion of OEDGE dealing with the impurity transport [18]. Both physical sputtering and chemical erosion are taken into account in DIVIMP and the eroded carbon particles are followed until they are deposited on the material surface. The local incident flux of C ions with different charge states and impact energy can be obtained. Figure 8(*a*) shows the carbon ion flux at different radial position from the simulations. The dominant species are C^{2+} and C^{3+} with similar flux to the surface. The W erosion by carbon neutrals is negligible since the carbon neutral flux is very small, with low impact energy. The calculated charge-state-resolved carbon ion flux has been implemented into the ERO code to simulate the W erosion and redeposition using the material mixing model. The W self-sputtering is also included in the modeling. As shown in figure 8(*b*), the ERO simulations well reproduce both the shape and the magnitude of the measured W gross erosion profile. The measured profile is shifted to the outboard direction by 8 mm, which is within the systematic uncertainty of the EFIT magnetic reconstruction. The inter-ELM W gross erosion rates can thus be well explained by impurity-induced W sputtering.

5. Summary

Significant advances have recently been made in the understanding of erosion and re-deposition of high-*Z* materials in

a mixed materials environment with a carbon wall in DIII-D. Various high-*Z* material coating samples have been exposed in well-diagnosed plasma discharges using the DiMES manipulator in DIII-D and analyzed by ion beam analysis and spectroscopic measurements. The roles of the sheath potential and background impurities in determining high-*Z* material erosion have been identified by comparison of experiments with modeling. Different methods suggested by modelling have been used to control high-*Z* material erosion. The Mo erosion is strongly suppressed by reducing the sheath potential drop using positive biasing. Local methane injection experiments verified the modeling results that high-*Z* material erosion could be reduced by increasing the background carbon impurity level. The $^{13}CH_4$ injection provides a good benchmark for modeling, demonstrating that the radial ^{13}C deposition profile on the Mo surface is strongly influenced by $\mathbf{E} \times \mathbf{B}$ drifts and cross-field diffusion. Local D_2 injection has been demonstrated as an effective means to reduce the W erosion rate via perturbation of local plasma conditions near the surface without affecting global plasma performance, due to lower sputtering yield and higher C deposition. In addition, spectroscopically measured radial profiles of inter-ELM W erosion rates in H-mode plasmas are well reproduced by ERO modeling taking into account charge-state-resolved carbon ion flux in the background plasma calculated using the OEDGE code. These studies may have significant implications for the understanding and active control of W divertor target operation in ITER with its low-*Z* beryllium first wall.

Acknowledgments

This material is based upon work supported by the US Department of Energy, Office of Science, Office of Fusion Energy Sciences and Office of Advanced Scientific Computing Research through the Scientific Discovery through Advanced Computing (SciDAC) project on Plasma-Surface Interactions, under Award No. GA-DE-SC0008698, using the DIII-D National Fusion Facility, a DOE Office of Science user facility, under Awards DE-AC05-06OR23100, DE-FG02-07ER54917, DE-AC05-00OR22725, DE-FC02-04ER54698 and DE-AC52-07NA27344. Sandia National Laboratories is a multi-program laboratory managed and operated by Sandia Corporation, a wholly owned subsidiary of Lockheed Martin Corporation, for the US Department of Energy's National Nuclear Security Administration under contract DE-AC04-94AL85000. DIII-D data shown in this paper can be obtained in digital format by following the links at https://fusion.gat.com/global/D3D_DMP. The first author acknowledges the supports by the National Magnetic Confinement Fusion Science Program of China under contract No 2013GB107004, the National Natural Science Foundation of China under Contract No 11375010, 11675218 and the Sino-German Center for Research Promotion under Contract No GZ769. D. Tskhakaya acknowledges the support by the project FWF P26544-N27.

References

[1] Pitts R.A. *et al* 2013 *J. Nucl. Mater.* **438** S48
[2] Kallenbach A. *et al* 2005 *Plasma Phys. Control. Fusion* **47** B207
[3] Brezinsek S. *et al* 2015 *J. Nucl. Mater.* **463** 11
[4] Den Harder N. *et al* 2016 *Nucl. Fusion* **56** 026014
[5] Dux R. *et al* 2009 *J. Nucl. Mater.* **390–1** 858
[6] Chankin A.V. *et al* 2014 *Plasma Phys. Control. Fusion* **56** 025003
[7] Tskhakaya D. *et al* 2015 *J. Nucl. Mater.* **463** 624
[8] Krieger K. *et al* 1999 *J. Nucl. Mater.* **266–9** 207
[9] Stangeby P.C. *et al* 2013 *J. Nucl. Mater.* **438** S309
[10] Wong C.P.C. *et al* 1998 *J. Nucl. Mater.* **258–63** 433
[11] Van Rooij G.J. *et al* 2013 *J. Nucl. Mater.* **438** S42
[12] Brezinsek S. *et al* 2011 *Phys. Scr.* **T145** 014016
[13] Wampler W.R. *et al* 2013 *J. Nucl. Mater.* **438** S822
[14] Rudakov D.L. *et al* 2014 *Phys. Scr.* **T159** 014030
[15] Ding R. *et al* 2016 *Nucl. Fusion* **56** 016021
[16] Brooks J.N. *et al* 2013 *J. Nucl. Mater.* **438** S673
[17] Kirschner A. *et al* 2000 *Nucl. Fusion* **40** 989
[18] Stangeby P.C. *et al* 2003 *J. Nucl. Mater.* **313–6** 883
[19] Kirschner A. *et al* 2009 *J. Nucl. Mater.* **390–1** 152
[20] Chodura R. 1982 *Phys. Fluids* **25** 1628
[21] Brooks J.N. 1990 *Phys. Fluids* B **2** 1858
[22] Stangeby P.C. 2012 *Nucl. Fusion* **52** 083012
[23] Rudakov D.L. *et al* 2015 *J. Nucl. Mater.* **463** 605
[24] Ding R. *et al* 2009 *Plasma Phys. Control. Fusion* **51** 055019
[25] Kirschner A. *et al* 2011 *J. Nucl. Mater.* **415** S23
[26] Ueda Y. *et al* 2009 *Nucl. Fusion* **49** 065027
[27] Aho-Mantila L. *et al* 2012 *Nucl. Fusion* **52** 103007
[28] Abrams T. *et al* 2017 *Nucl. Fusion* at press